Parametric Type-II Dirac Photonic Lattices

*Kaichao Jin, Hua Zhong, Yongdong Li, Fangwei Ye, Yanpeng Zhang, Fuli Li, Chunliang Liu,
and Yiqi Zhang**

Different from the Fermi surface of the type-I Dirac semimetal being a point,
that of the type-II Dirac semimetal is a pair of crossing lines because the Dirac
cone is tilted with open and hyperbolic isofrequency contours. As an optical
analogy, type-II Dirac photonic lattices have been also designed. Here, type-II
Dirac cones are reported in Lieb-like photonic lattices composed of identical
waveguide channels, and the anisotropy of the band structure is due to
neither the refractive index change nor the environment, but only the spatial
symmetry of the lattice; therefore, the proposal is advantageous and benefits
experimental observation. Conical diffractions and Klein tunneling in the
parametric type-II photonic lattice are investigated in detail. The results
provide a simple and experimentally feasible platform to study
two-dimensional topological photonic and other nonrelativistic phenomena
around type-II Dirac cones.

If a photonic lattice possesses Dirac cones[1] in its structure, it can be called a Dirac photonic lattice . One of the most famous Dirac photonic lattices is the photonic graphene,[2–9] which is also known as the honeycomb lattice. In addition, the Lieb lattice,[10–15] the kagome lattice,[16,17] the superhoneycomb lattices,[18,19] and some others[20] can be also classified into Dirac photonic lattices. It is worth mentioning that the Dirac cones of these photonic lattices aforementioned are mostly type-I, even though some of them are tilted. Actually, there are also type-II and type-III Dirac cones.[21] The main difference between them is that

K. C. Jin, H. Zhong, Prof. Y. D. Li, Prof. Y. P. Zhang, Prof. C. L. Liu,
Dr. Y. Q. Zhang
Key Laboratory for Physical Electronics and Devices of the Ministry of
Education & Shaanxi Key Lab of Information Photonic Technique
Xi'an Jiaotong University
Xi'an 710049, China
E-mail: zhangyiqi@mail.xjtu.edu.cn
K. C. Jin, H. Zhong, Dr. Y. Q. Zhang
Guangdong Xi'an Jiaotong University Academy
Foshan 528300, China
Prof. F. W. Ye
School of Physics and Astronomy
Shanghai Jiao Tong University
Shanghai 200240, China
Prof. F. L. Li
Department of Applied Physics
School of Science
Xi'an Jiaotong University
Xi'an 710049, China

The ORCID identification number(s) for the author(s) of this article
can be found under https://doi.org/10.1002/qute.202000015

the Fermi surface of the type-I Dirac cone is a point, that of the type-II Dirac cone is a pair of crossing lines, and that of the type-III Dirac cone is a line. In other words, the isofrequency contours of the type-I Dirac cones are closed, while those of the type-II counterparts are open and have hyperbolic profiles (e.g., on both $+k_y$- and $-k_y$-directions). The isofrequency contours of the type-III ones are also open, but only have hyperbolic profiles on one side (e.g., on either $+k_y$- or $-k_y$-direction). Note that there is also a different definition on the type-III degeneracy.[22] As a plethora of efforts are being implemented to explore the type-II Weyl-like features[23–29] both in condensed matter physics and photonics, type-II Dirac objects attract ongoing attentions too,[30–36] especially in photonics.[21,37–41] Different from ubiquitous type-I Dirac cones, appearance of type-II Dirac cones demands either high anisotropic lattice arrangement or accurate manipulation of the lattice environment. Despite the difference, quasiparticles corresponding to both the two types of Dirac cones are massless, and can be described by the massless Dirac Hamiltonian,[42] thereby Dirac materials become unique paradigms to explore relativistic Dirac-related phenomena, such as Klein tunneling.[43]

Being a relativistic phenomenon, Klein tunneling means that a massless particle can overpass a barrier higher than its energy freely. Surprisingly, this nonintuitive prediction was also explained successfully in the frame of classical electromagnetic theory and simulated and observed in classical systems, such as deformed honeycomb lattice,[44,45] waveguide superlattices,[46,47] matamaterials,[48] and pseudospin-1 photonic crystals.[49] As far as we know, Klein tunneling in type-II Dirac photonic lattices is still open to be explored.

In this work, we unveil type-II Dirac cones in novel but simple lattice waveguide arrays constructed by identical waveguide channels that are transversely arranged in morphable lattice profiles with three sites in one unit cell, via a controllable angle parameter θ in the range $[\pi/6, \pi]$ (**Figure 1**). When the angle reaches its supreme value, a dislocated Lieb lattice[50] that has both type-I and type-III Dirac cones[21] is created. With the angle value decreased, the lattice deforms with the type-III Dirac cones reducing into tilted type-I Dirac cones. Further deformation of the lattice by reducing the angle value, the type-I Dirac cones tilt even further and evolve into the type-II Dirac cones gradually. Light modulation and manipulation based on these various Dirac cones are elucidated by the corresponding conical diffractions, and for the first time, the Klein tunneling is demonstrated in the type-II Dirac

**ADVANCED
SCIENCE NEWS**
www.advancedsciencenews.com

**ADVANCED
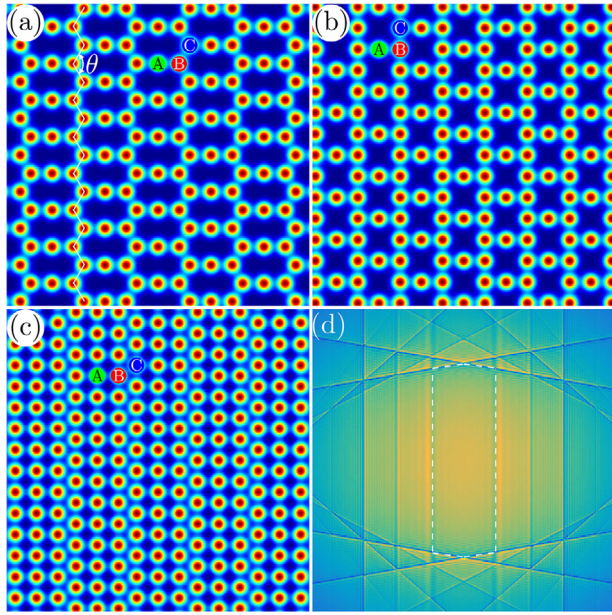QUANTUM
TECHNOLOGIES**
www.advquantumtech.com

Figure 1. a) Lattice with a controllable parameter θ. Here, $\theta = 2\pi/3$. b) Lattice with $\theta = \pi$, which is also the dislocated Lieb lattice. c) Lattice with $\theta = \pi/3$. d) Far-field diffraction pattern of the lattice in (c). The first Brillouin zone is shown by the dashed deformed hexagon. Unit cell of the lattice includes three sites that are indicated by green, red, and blue colors with letters A, B, and C. Other parameters: $a = 1.4$, $p = 10$, and $d = 0.5$.

photonic lattice. Our results provide a new design for type-II Dirac photonic lattices, which has advantage of simplicity since the appearance of the type-II Dirac cones is only dependent on the spatial symmetry of the lattice.

Propagation of a light beam in a photonic lattice waveguide array can be faithfully described by the Schrödinger-like paraxial wave equation:

$$i\frac{\partial \psi}{\partial z} = -\frac{1}{2}\left(\frac{\partial^2}{\partial x^2} + \frac{\partial^2}{\partial y^2}\right)\psi - \mathcal{R}(x,y)\psi \tag{1}$$

where the transverse (x, y) and longitudinal z-coordinates are normalized to the characteristic transverse scale r_0 and the diffraction length $L_{\text{dif}} = kr_0^2$, respectively; $k = 2\pi n_0/\lambda$ is the wavenumber with n_0 being the background refractive index and λ the wavelength. The lattice potential $\mathcal{R}(x, y) = p\sum_{n,m}\mathcal{Q}(x - x_n, y - y_m)$ is composed of Gaussian waveguides $\mathcal{Q} = \exp(-x^2/a_x^2 - y^2/a_y^2)$ with p being the depths of two sublattices, $a_{x,y}$ waveguide widths, and (x_n, y_m) the transverse location of each waveguide channel. The lattice constant is labeled as d which is the distance between two nearest-neighbor sites. The photonic lattice can be prepared by using, for instance, the femtosecond laser writing technique in fused silica material[51–53] and the optically induced technique in photorefractive crystals.[8,15,54] Taking the former technique as an example, one can use the following parameters: $\lambda = 633$ nm, $d = 15\,\mu\text{m}$, $a_x = a_y = 10\,\mu\text{m}$. If we choose the transverse scale $r_0 = 10\,\mu\text{m}$, the diffraction length $L_{\text{dif}} = 1.4$ mm. The lattice depth $p = 10$ corresponds to refractive index change of 7×10^{-4} in a real physical system.

The solution of Equation (1) can be written as $\psi(x, y, z) = u(x, y)\exp(i\beta z)$ with β being the propagation constant (or "en-

ergy" of the quasiparticle) and $u(x, y)$ the Bloch mode. Plugging this solution into Equation (1), one obtains

$$\beta u = \frac{1}{2}\left(\frac{\partial^2}{\partial x^2} + \frac{\partial^2}{\partial y^2}\right)u + \mathcal{R}(x, y)u \tag{2}$$

which can be solved numerically by using the plane-wave expansion method. As a periodic function of Bloch momenta $k_{x,y}$, $\beta(k_x, k_y)$ is the band structure of the photonic lattice $\mathcal{R}(x, y)$. Clearly, photonic lattices with different geometries possess different band structures.[55] One may see the lattice transverse profile shown in Figure 1a, which possesses three sites (labeled as A, B, and C) in one unit cell. Now, we introduce another controlling parameter, the angle θ between sites B and C along vertical y-direction, as shown by the zigzag line. Here in Figure 1a, the angle $\theta = 2\pi/3$. If the angle $\theta = \pi$, one obtains the dislocated Lieb lattice,[50] as shown in Figure 1b, which is different from the traditional Lieb lattice.[11,12] One can change the angle continuously to deform the lattice, and in Figure 1c, the lattice with $\theta = \pi/3$ is shown. It is convenient to check the far-field diffraction patterns[56] of the lattices, which can show the corresponding Brillouin zones directly. According to numerical simulations, one may find that the first Brillouin zones are deformed hexagons, and the smaller the angle, the larger the deformation of the hexagons. In Figure 1d, we only show the far-field diffraction pattern of the lattice shown in Figure 1c. Since the first Brillouin zone is always a hexagon, there must be always three sites in one unit cell no matter what the value of the angle. Even though there are still three sites in one unit cell in the lattice with $\theta = \pi/3$, the property may change greatly in comparison with those with $\theta = 2\pi/3$ and $\theta = \pi$. An explicit fact is that under the tight-binding approximation, there are 2, 3, and 3 nearest-neighbor sites for sites A, B, and C, respectively, both in Figures 1a and 1b. However in Figure 1c, the numbers are 4, 5, and 5. According to the geometry of the lattice in Figure 1c, the locations of the six corners of the first Brillouin zone can be obtained theoretically as

$$\left(0, \pm\frac{(20 + 8\sqrt{3})\pi}{(19 + 8\sqrt{3})a}\right) \quad \text{and} \quad \left(\pm\frac{2\pi}{(4 + \sqrt{3})a}, \pm\frac{(18 + 8\sqrt{3})\pi}{(19 + 8\sqrt{3})a}\right)$$

which are in accordance with the numerical results in Figure 1d.

By solving Equation (2) numerically, we obtain the band structures for the lattices in Figure 1, which are displayed in **Figure 2**. In Figure 2a that corresponds to the lattice with $\theta = 2\pi/3$ in Figure 1a, all the Dirac cones are tilted type-I. While in Figure 2b that corresponds to Figure 1b, the Dirac cones between the top and bottom bands are tilted type-I, but those between the middle and bottom bands are type-III. When the angle decreases successively to $\theta = \pi/3$, as shown in Figure 2c, all the Dirac cones become type-II, because the group velocity along y (i.e., $-d\beta/dk_y$) of the mode around the Dirac points does not change sign.

To understand the emergence of the type-II Dirac cones, we theoretically analyze the couplings among sites in Figure 1c by adopting the tight-binding approximation method and only
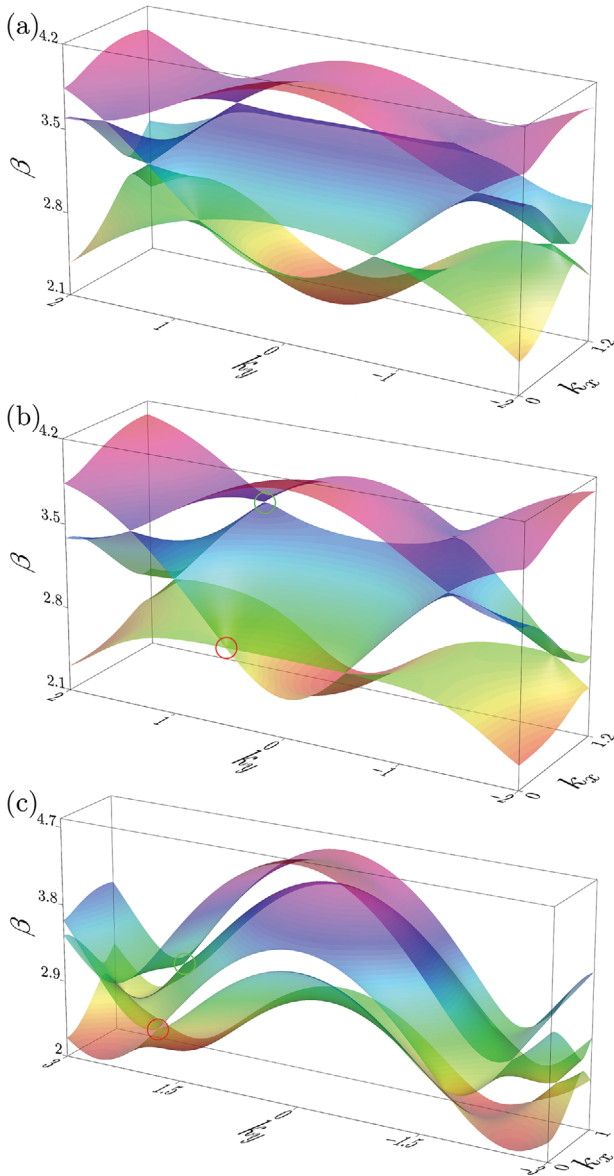
ADVANCED
SCIENCE NEWS
www.advancedsciencenews.com

ADVANCED
QUANTUM
TECHNOLOGIES
www.advquantumtech.com

Figure 2. a–c) Two-dimensional band structures corresponding to Figure 1a–c.

considering the nearest-neighbor interaction. The corresponding Hamiltonian can be written as

$$
H = t \begin{bmatrix} 2\cos(\mathbf{k} \cdot \mathbf{e}_2) & e^{i\mathbf{k} \cdot \mathbf{e}_1} & e^{-i\mathbf{k} \cdot \mathbf{e}_1} \\ e^{-i\mathbf{k} \cdot \mathbf{e}_1} & 2\cos(\mathbf{k} \cdot \mathbf{e}_2) & e^{i\mathbf{k} \cdot \mathbf{e}_3} + e^{i\mathbf{k} \cdot \mathbf{e}_4} \\ e^{i\mathbf{k} \cdot \mathbf{e}_1} & e^{-i\mathbf{k} \cdot \mathbf{e}_3} + e^{-i\mathbf{k} \cdot \mathbf{e}_4} & 2\cos(\mathbf{k} \cdot \mathbf{e}_2) \end{bmatrix} \quad (3)
$$

in which $\mathbf{k} = [k_x, k_y]$, $\mathbf{e}_1 = [a, 0]$, $\mathbf{e}_2 = [0, a]$, $\mathbf{e}_3 = [\sqrt{3}a/2, a/2]$, $\mathbf{e}_4 = [\sqrt{3}a/2, -a/2]$, and t the coupling strength. The eigenvalues of Equation (3) are the band structure, but the analytical solution is hard to obtain. Even so, one still can obtain the locations of the Dirac points, which are $[0, \pm 4\pi/3a]$ and $[\pm 2\pi/(4 + \sqrt{3})a, \pm 2\pi/3a]$ between the top and middle bands, and $[0, \pm 2\pi/3a]$ and $[\pm 2\pi/(4 + \sqrt{3})a, \pm 4\pi/3a]$ between the mid-

dle and bottom bands. Numerical band structure is displayed in **Figure 3**a, which looks visually the same with that in Figure 2c although quantitatively there are differences in the value of β. Since all the Dirac cones are type-II for this case, we take the Dirac point at $[0, 4\pi/3a]$ as an example without loss of generality, and this Dirac cone is shown in the inset of Figure 3a. Before going into a subtle theoretical analysis on this type-II Dirac cone, it is necessary to have a look at the corresponding cross sections in the (k_x, k_y) plane with $\beta = 0$ (Figure 3b), the (k_y, β) plane with $k_x = 0$ (Figure 3c), and the (k_x, β) plane with $k_y = 4\pi/3a$ (Figure 3d). In the $\beta = 0$ plane, the intersection of the top and middle bands, as shown in Figure 3b, exhibits two crossing lines.[21,23] In Figure 3c, the red and blue lines show the profile of the Dirac cone in the cross section $k_x = 0$ which clearly elucidates that the sign of the slope $d\beta/dk_y$ does not change along k_y-direction. While in Figure 3d, the profile of the Dirac cone in the cross section $k_y = 0$ is symmetric about $k_x = 0$ (i.e., sign of $d\beta/dk_x$ changes), which is similar to that for a (tilted) type-I Dirac points. To this regard, if we expand the Hamiltonian in the infinitesimal region $(p_x = k_x - k_x^D, p_y = k_y - k_y^D)$ around the Dirac point (k_x^D, k_y^D), we can only consider the component along k_y-direction and let $p_x = 0$ safely. As a result, the corresponding Hamiltonian can be written as

$$
H = t \begin{bmatrix} \sqrt{3}ap_y - 1 & 1 & 1 \\ 1 & \sqrt{3}ap_y - 1 & -\frac{\sqrt{3}}{2}ap_y - 1 \\ 1 & -\frac{\sqrt{3}}{2}ap_y - 1 & \sqrt{3}ap_y - 1 \end{bmatrix} \quad (4)
$$

The eigenvalues of this Hamiltonian are

$$
\beta_1 = \frac{3}{2}\sqrt{3}atp_y, \ \beta_2 = \frac{5}{6}\sqrt{3}atp_y, \ \beta_3 = \frac{2}{3}\sqrt{3}atp_y - 3t \quad (5)
$$

Clearly, one may find the relation $\beta_1|_{p_y=0} = \beta_2|_{p_y=0} = 0$, which indicates that the two bands are degenerated at the point ($p_x = 0$, $p_y = 0$)—the location of the Dirac point. One also finds that $d\beta_1/dp_y$ and $d\beta_2/dp_y$ always have the same sign, therefore the velocity does not change its sign around the Dirac point, and the Dirac cone is type-II definitely.

If the incident beam can excite the Dirac cone states properly, the beam will undergo conical diffraction during propagation.[1,13,18–20,57,58] Since there are type-I, type-II, and type-III Dirac cones in Figures 2b and 2c, we do not consider the Dirac cones in Figure 2a and only excite these Dirac cone states indicated by green and red circles, which can be achieved via the method developed in refs. [19,20]. After propagating a distance of $z = 200$, the output intensity profiles of these excited Dirac cone states are displayed in **Figure 4**, in which the dotted circles represent the location and size of the input Dirac cone states, and the vertical and horizontal dashed yellow lines are the $x = 0$ and $y = 0$ axes, respectively.

Corresponding to the tilted type-I Dirac cone surrounded by the green circle in Figure 2b, the conical diffraction is displayed in Figure 4a. Due to the tilt of the Dirac cone, the diffraction speeds along $+y$- and $-y$-directions are different, so the diffraction ring exhibits an elliptic profile. If the type-III Dirac cone state is excited, as indicated by the red circle in Figure 2b, the conical diffraction may only happen along $-y$-direction, because the
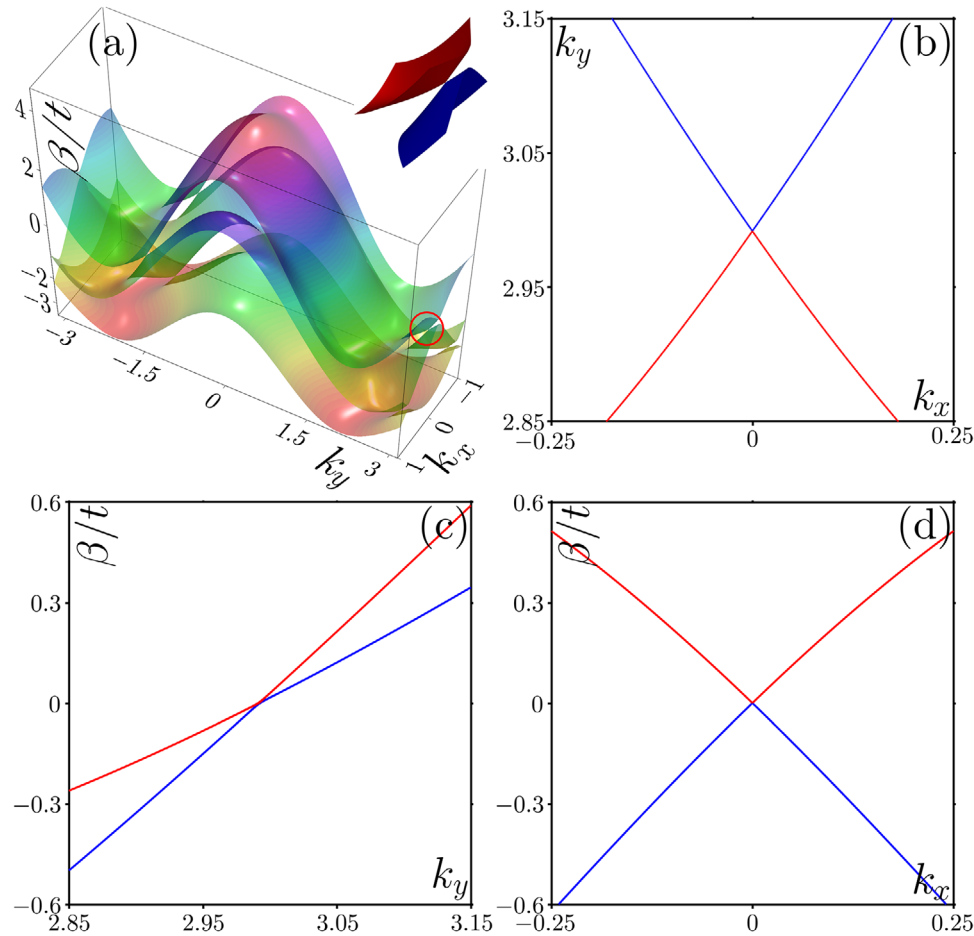
**ADVANCED
SCIENCE NEWS**
www.advancedsciencenews.com

**ADVANCED
QUANTUM
TECHNOLOGIES**
www.advquantumtech.com

Figure 3. a) Band structure according to Equation (3). The red circle labels the type-II Dirac point that is investigated, and its corresponding magnification is displayed in the inset. In the inset, the top and middle bands are in red and blue colors, respectively. b) Cross section of the Dirac cone in the (k_x, k_y) plane with $\beta = 0$. c) Cross section of the Dirac cone in the (k_y, β) plane with $k_x = 0$. d) Cross section of the Dirac cone in the (k_x, β) plane with $k_y = 4\pi/3a$. In (b–d), colors of the lines are in accordance with those of the bands in the inset in (a).

group velocity along $+\gamma$-direction $-d\beta/dk_y \approx 0$. The numerical result is shown in Figure 4b, and indeed, the diffraction ring only appears in the $-\gamma$ region with the location of the upper edge of the ring nearly being invariant. Different from the type-I and type-III Dirac cones, the sign of speed $-d\beta/dk_y$ of the type-II Dirac cone does not change along γ-coordinate, so the whole conical diffraction ring will move along either $+\gamma$- or $-\gamma$-direction. As to the type-II Dirac cones marked with green and red circles in Figure 2c, conical diffraction rings will move along $+\gamma$-direction because of $-d\beta/dk_y > 0$, and the corresponding numerical simulations are displayed in Figures 4c and 4d. Considering that all the Dirac cones are tilted along k_y-coordinate only, the conical diffractions in Figure 4 are symmetric about $x = 0$. Note that the diameter of the diffraction ring along x-coordinate in Figure 4d is much bigger than that in Figure 4c, and the reason is that the absolute value of $-d\beta/dk_x$ of the Dirac cone surrounded by the green circle is smaller than that of the Dirac cone surrounded by the red circle. In short, the spatial conical diffraction patterns can be predicted from the profiles of the Dirac cones, and vice versa, the properties of the Dirac cones are manifested into the conical diffraction patterns.

Different from ordinary quantum mechanical tunneling, the term Klein tunneling refers to a counterintuitive relativistic process in which an electron can penetrate through a potential barrier higher than the electron's rest energy.[43] Since conical diffraction due to the type-II Dirac cones moves along $+\gamma$-direction spontaneously even with zero incident angle, it becomes an ideal paradigm to investigate the Klein tunneling. This is indeed more advantage than that in type-I Dirac photonic lattices, where the movement of the incident beam is required through tuning the angle of incidence. What one is required to do is setting up a barrier in the type-II Dirac photonic lattice at a proper place where the conical diffraction will move toward. Generally, the lattice potential superimposed with a barrier can be written as

$$\mathcal{R}(x, \gamma) = \begin{cases} \mathcal{R}(x, \gamma) & \text{if } \gamma \leq \gamma_1 \text{ or } \gamma > \gamma_2, \\ \mathcal{R}(x, \gamma) + h & \text{if } \gamma_1 < \gamma \leq \gamma_2 \end{cases} \qquad (6)$$

in which $h > 0$ is the height and $\gamma_2 - \gamma_1$ is the width of the barrier. The type-II Dirac photonic lattice with a barrier is shown in **Figure 5**a, and the incident type-II Dirac cone state

**ADVANCED
SCIENCE NEWS**

www.advancedsciencenews.com

**ADVANCED
QUANTUM
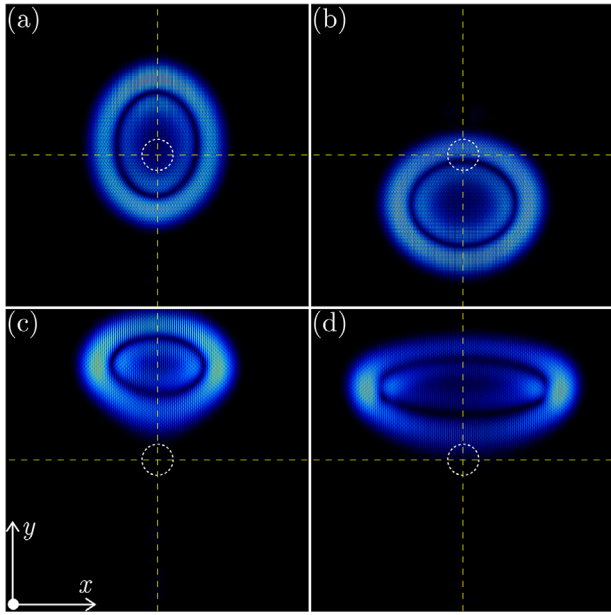TECHNOLOGIES**

www.advquantumtech.com

Figure 4. a) Conical diffraction due to the tilted type-I Dirac cone marked by the green circle in Figure 2b. b) Conical diffraction due to the type-III Dirac cone marked by the red circle in Figure 2b. c) Conical diffraction due to the type-II Dirac cone marked by the green circle in Figure 2c. d) Conical diffraction due to the type-II Dirac cone marked by the red circle in Figure 2c. All panels are in the range $-300 \leq x, y \leq 300$. Dashed lines are along $x = 0$ and $y = 0$. Dotted circles in each panel represent the input beams.
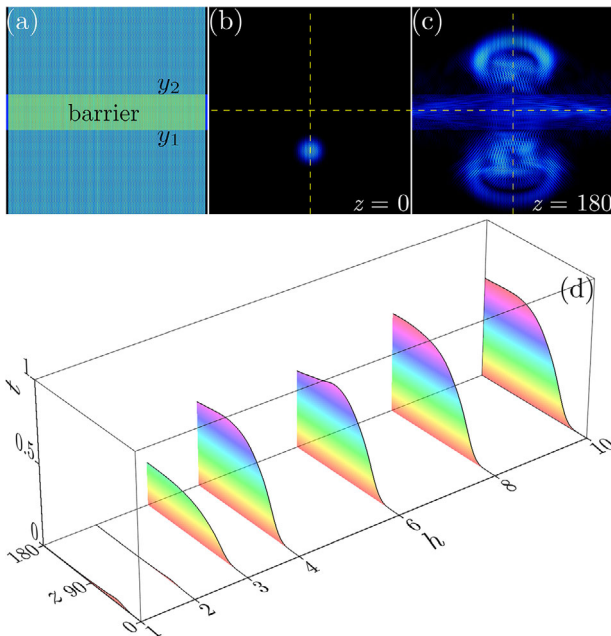

Figure 5. a) Type-II photonic lattice with a barrier. b) Input type-II Dirac state superimposed with a wide Gaussian, which is same as those used in Figure 4 but with the beam center locating at $(0, -120)$. c) Output of the beam which exhibits Klein tunneling with $h = 10$, $y_1 = -58$, and $y_2 = 48$. d) Klein tunneling with different height of the barrier. Panels in (b,c) are in the range $-300 \leq x, y \leq 300$, and dashed lines are along $x = 0$ and $y = 0$.

(corresponding to the Dirac cone marked with the green circle in Figure 2c) superimposed with a wide Gaussian that is placed below the barrier is displayed in Figure 5b. The incident state will exhibit conical diffraction during propagation, and meanwhile, the conical diffraction pattern moves upward along $+y$-direction, as in Figure 4c. Inevitably, the conical diffraction pattern will hit on the barrier, and it will be reflected by the barrier by intuition. Nevertheless, transmission of the conical diffraction pattern over the barrier is completely possible if the barrier height is bigger than 3—a requirement of Klein tunneling, because the "energy" of the state at the Dirac point marked with the green circle in Figure 2c is about $\beta \approx 3$. To track the Klein tunneling process, we define a physical quantity named the transmission ratio, as

$$r = \frac{P_{KT}}{P}$$

with

$$P = \int_{-\infty}^{+\infty} \int_{-\infty}^{+\infty} |\psi|^2 dx \, dy$$

and

$$P_{KT} = \int_{-\infty}^{+\infty} \int_{y_1}^{+\infty} |\psi|^2 dx \, dy$$

The transmission ratio t as a function of propagation distance z for barriers with different height is shown in Figure 5d. Distinctly, the conical diffraction is almost reflected by the barrier when the height is smaller than the "energy"; see the curves corresponding to $h = 1, 2$ in Figure 5d. Klein tunneling starts to happen if the barrier height is close to the "energy," and this is demonstrated by the curve with $h = 3$. Increasing the barrier height further, the transmission ratio also grows, but numerical simulations indicate that there is seemingly a saturable value for the transmission ratio, which is $\sim 70\%$. The reason for not reaching the perfect Klein tunneling is due to that the incident beam in Figure 5b is not really "massless." On one hand, the Dirac cone state is approximately obtained and its corresponding Bloch momentum is not exactly in the infinitesimal region around the critical point. On the other hand, the superimposed wide Gaussian beam is a "massive" object. The output amplitude profile with $h = 10$ is displayed in Figure 5c, which clearly manifests the Klein tunneling of the conical diffraction. Since the conical diffraction still holds after penetrating the barrier, excitation of the type-II Dirac cone mode is conserved.

Note that the steps of the barrier given by Equation (6) are sharp. If this barrier is replaced by one with smooth steps, for example, a super-Gaussian, which transforms the potential into

$$\mathcal{R}(x, y) = \mathcal{R}(x, y) + h \exp(-y^8/w^8)$$

with $w = 50$, one will not miss out on the finding that the Klein tunneling is completely inhibited, which also demonstrates that the phenomenon reported in Figure 5 is truly Klein tunneling. The explanation of this inhibition is that the barrier with smooth steps can be regarded as a combination of sub-barriers with sharp steps, infinitesimal width, and different height. The conical diffraction will first encounter the sub-barrier with very small

**ADVANCED
SCIENCE NEWS**

www.advancedsciencenews.com

**ADVANCED
QUANTUM
TECHNOLOGIES**

www.advquantumtech.com

height upon its movement along +y-direction, and this height is always smaller than the "energy" of the conical diffraction beam which dissatisfies the requirement of appearance of the Klein tunneling.

Summarizing, we have constructed a type-II Dirac photonic lattice from the Lieb-like lattice by simply adjusting a angle parameter which only changes the spatial symmetry of the lattice. Conical diffraction and Klein tunneling in this novel type-II Dirac photonic lattice are discussed in detail. We believe that our results may not only provide a feasible avenue on light manipulation, but also help realize other topological photonic and analogize non-relativistic phenomena in photonic lattices. In addition to photonics, we believe that the developed type-II Dirac lattice in this work may also provide a completely new flatform for cold atoms and acoustics.

A paper[59] on constructing type-II Dirac points by proposing a band-folding scheme, and a paper[60] on symmetry-controlled edge states in the type-II phase of Dirac photonic lattices, were published after submission of this paper. We would like to emphasize that, in our work for the first time, we find the simplest way to construct type-II Dirac points which only depends on the spatial symmetry of the photonic lattice.

Conflict of Interest

The authors declare no conflict of interest.

[1] D. Leykam, A. S. Desyatnikov, *Adv. Phys. X* **2016**, *1*, 101.
[2] S. R. Zandbergen, M. J. A. de Dood, *Phys. Rev. Lett.* **2010**, *104*, 043903.
[3] M. C. Rechtsman, Y. Plotnik, J. M. Zeuner, D. Song, Z. Chen, A. Szameit, M. Segev, *Phys. Rev. Lett.* **2013**, *111*, 103901.
[4] M. C. Rechtsman, J. M. Zeuner, A. Tünnermann, S. Nolte, M. Segev, A. Szameit, *Nat. Photon.* **2013**, *7*, 153.
[5] A. Crespi, G. Corrielli, G. D. Valle, R. Osellame, S. Longhi, *New J. Phys.* **2013**, *15*, 013012.
[6] J. M. Zeuner, M. C. Rechtsman, S. Nolte, A. Szameit, *Opt. Lett.* **2014**, *39*, 602.
[7] Y. Plotnik, M. C. Rechtsman, D. Song, M. Heinrich, J. M. Zeuner, S. Nolte, Y. Lumer, N. Malkova, J. Xu, A. Szameit, Z. Chen, M. Segev, *Nat. Mater.* **2014**, *13*, 57.
[8] D. Song, V. Paltoglou, S. Liu, Y. Zhu, D. Gallardo, L. Tang, J. Xu, M. Ablowitz, N. K. Efremidis, Z. Chen, *Nat. Commun.* **2015**, *6*, 6272.
[9] A. V. Nalitov, G. Malpuech, H. Terças, D. D. Solnyshkov, *Phys. Rev. Lett.* **2015**, *114*, 026803.
[10] S. Taie, H. Ozawa, T. Ichinose, T. Nishio, S. Nakajima, Y. Takahashi, *Sci. Adv.* **2015**, *1*, 1500854.
[11] R. A. Vicencio, C. Cantillano, L. Morales-Inostroza, B. Real, C. Mejía-Cortés, S. Weimann, A. Szameit, M. I. Molina, *Phys. Rev. Lett.* **2015**, *114*, 245503.
[12] S. Mukherjee, A. Spracklen, D. Choudhury, N. Goldman, P. Öhberg, E. Andersson, R. R. Thomson, *Phys. Rev. Lett.* **2015**, *114*, 245504.
[13] F. Diebel, D. Leykam, S. Kroesen, C. Denz, A. S. Desyatnikov, *Phys. Rev. Lett.* **2016**, *116*, 183902.
[14] H. Ozawa, S. Taie, T. Ichinose, Y. Takahashi, *Phys. Rev. Lett.* **2017**, *118*, 175301.
[15] S. Xia, A. Ramachandran, S. Xia, D. Li, X. Liu, L. Tang, Y. Hu, D. Song, J. Xu, D. Leykam, S. Flach, Z. Chen, *Phys. Rev. Lett.* **2018**, *121*, 263902.
[16] A. El Hassan, F. K. Kunst, A. Moritz, G. Andler, E. J. Bergholtz, M. Bourennane, *Nat. Photon.* **2019**, *13*, 697.
[17] M. Li, D. Zhirihin, M. Gorlach, X. Ni, D. Filonov, A. Slobozhanyuk, A. Alù, A. B. Khanikaev, *Nat. Photon.* **2019**.
[18] H. Zhong, Y. Q. Zhang, Y. Zhu, D. Zhang, C. B. Li, Y. P. Zhang, F. L. Li, M. R. Belić, M. Xiao, *Ann. Phys. (Berlin)* **2017**, *529*, 1600258.
[19] Y. F. Kang, H. Zhong, M. R. Belić, Y. Q. Tian, K. C. Jin, Y. P. Zhang, F. L. Li, Y. Q. Zhang, *Ann. Phys. (Berlin)* **2019**, *531*, 1900295.
[20] H. Zhong, R. Wang, M. R. Belić, Y. P. Zhang, Y. Q. Zhang, *Opt. Express* **2019**, *27*, 6300.
[21] M. Milićević, G. Montambaux, T. Ozawa, O. Jamadi, B. Real, I. Sagnes, A. Lemaître, L. Le Gratiet, A. Harouri, J. Bloch, A. Amo, *Phys. Rev. X* **2019**, *9*, 031010.
[22] X. P. Li, K. Deng, B. Fu, Y. Li, D. Ma, J. Han, J. Zhou, S. Zhou, Y. Yao, arXiv:1909.12178 [cond-mat.mes-hall], **2019**.
[23] A. A. Soluyanov, D. Gresch, Z. Wang, Q. Wu, M. Troyer, X. Dai, B. A. Bernevig, *Nature* **2015**, *527*, 495.
[24] Y. Xu, F. Zhang, C. Zhang, *Phys. Rev. Lett.* **2015**, *115*, 265304.
[25] W. J. Chen, M. Xiao, C. T. Chan, *Nat. Commun.* **2016**, *7*, 13038.
[26] G. Autès, D. Gresch, M. Troyer, A. A. Soluyanov, O. V. Yazyev, *Phys. Rev. Lett.* **2016**, *117*, 066402.
[27] J. Noh, S. Huang, D. Leykam, Y. Chong, K. P. Chen, M. Rechtsman, *Nat. Phys.* **2017**, *13*, 611.
[28] R. Chen, B. Zhou, D. H. Xu, *Phys. Rev. B* **2018**, *97*, 155152.
[29] B. Xie, H. Liu, H. Cheng, Z. Liu, S. Chen, J. Tian, *Phys. Rev. Lett.* **2019**, *122*, 104302.
[30] M. Yan, H. Huang, K. Zhang, E. Wang, W. Yao, K. Deng, G. Wan, H. Zhang, M. Arita, H. Yang, Z. Sun, H. Yao, Y. Wu, S. Fan, W. Duan, S. Zhou, *Nat. Commun.* **2017**, *8*, 257.
[31] H. J. Noh, J. Jeong, E. J. Cho, K. Kim, B. I. Min, B. G. Park, *Phys. Rev. Lett.* **2017**, *119*, 016401.
[32] T. R. Chang, S. Y. Xu, D. S. Sanchez, W. F. Tsai, S. M. Huang, G. Chang, C. H. Hsu, G. Bian, I. Belopolski, Z. M. Yu, S. A. Yang, T. Neupert, H. T. Jeng, H. Lin, M. Z. Hasan, *Phys. Rev. Lett.* **2017**, *119*, 026404.
[33] F. Fei, X. Bo, P. Wang, J. Ying, J. Li, K. Chen, Q. Dai, B. Chen, Z. Sun, M. Zhang, F. Qu, Y. Zhang, Q. Wang, X. Wang, L. Cao, H. Bu, F. Song, X. Wan, B. Wang, *Adv. Mater.* **2018**, *30*, 1801556.
[34] A. Politano, G. Chiarello, B. Ghosh, K. Sadhukhan, C. N. Kuo, C. S. Lue, V. Pellegrini, A. Agarwal, *Phys. Rev. Lett.* **2018**, *121*, 086804.
[35] D. Kim, S. Ahn, J. H. Jung, H. Min, J. Ihm, J. H. Han, Y. Kim, *Phys. Rev. Mater.* **2018**, *2*, 104203.
[36] B. Wang, H. Gao, Q. Lu, W. Xie, Y. Ge, Y. H. Zhao, K. Zhang, Y. Liu, *Phys. Rev. B* **2018**, *98*, 115164.
[37] J. Y. Lin, N. C. Hu, Y. J. Chen, C. H. Lee, X. Zhang, *Phys. Rev. B* **2017**, *96*, 075438.

**ADVANCED
SCIENCE NEWS**

www.advancedsciencenews.com

**ADVANCED
QUANTUM
TECHNOLOGIES**

www.advquantumtech.com

[38] G. G. Pyrialakos, N. S. Nye, N. V. Kantartzis, D. N. Christodoulides, *Phys. Rev. Lett.* **2017**, *119*, 113901.

[39] H. X. Wang, Y. Chen, Z. H. Hang, H. Y. Kee, J. H. Jiang, *npj Quantum Mater.* **2017**, *2*, 54.

[40] C. Hu, Z. Li, R. Tong, X. Wu, Z. Xia, L. Wang, S. Li, Y. Huang, S. Wang, B. Hou, C. T. Chan, W. Wen, *Phys. Rev. Lett.* **2018**, *121*, 024301.

[41] C. R. Mann, T. J. Sturges, G. Weick, W. L. Barnes, E. Mariani, *Nat. Commun.* **2018**, *9*, 2194.

[42] S. Li, Z. M. Yu, Y. Liu, S. Guan, S. S. Wang, X. Zhang, Y. Yao, S. A. Yang, *Phys. Rev. B* **2017**, *96*, 081106.

[43] M. I. Katsnelson, K. S. Novoselov, A. K. Geim, *Nat. Phys.* **2006**, *2*, 620.

[44] O. Bahat-Treidel, O. Peleg, M. Grobman, N. Shapira, M. Segev, T. Pereg-Barnea, *Phys. Rev. Lett.* **2010**, *104*, 063901.

[45] O. Bahat-Treidel, M. Segev, *Phys. Rev. A* **2011**, *84*, 021802.

[46] S. Longhi, *Phys. Rev. B* **2010**, *81*, 075102.

[47] F. Dreisow, R. Keil, A. Tünnermann, S. Nolte, S. Longhi, A. Szameit, *EPL* **2012**, *97*, 10008.

[48] L. Sun, J. Gao, X. Yang, *Sci. Rep.* **2017**, *7*, 9678.

[49] A. Fang, Z. Q. Zhang, S. G. Louie, C. T. Chan, *Research* **2019**, *2019*, 3054062.

[50] C. Li, F. Ye, X. Chen, Y. V. Kartashov, A. Ferrando, L. Torner, D. V. Skryabin, *Phys. Rev. B* **2018**, *97*, 081103.

[51] M. C. Rechtsman, J. M. Zeuner, Y. Plotnik, Y. Lumer, D. Podolsky, F. Dreisow, S. Nolte, M. Segev, A. Szameit, *Nature* **2013**, *496*, 196.

[52] S. Stützer, Y. Plotnik, Y. Lumer, P. Titum, N. H. Lindner, M. Segev, M. C. Rechtsman, A. Szameit, *Nature* **2018**, *560*, 461.

[53] E. Lustig, S. Weimann, Y. Plotnik, Y. Lumer, M. A. Bandres, A. Szameit, M. Segev, *Nature* **2019**, *567*, 356.

[54] P. Wang, Y. Zheng, X. Chen, C. Huang, Y. V. Kartashov, L. Torner, V. V. Konotop, F. Ye, *Nature* **2020**, *577*, 42.

[55] L. Tarruell, D. Greif, T. Uehlinger, G. Jotzu, T. Esslinger, *Nature* **2012**, *483*, 302.

[56] G. Bartal, O. Cohen, H. Buljan, J. W. Fleischer, O. Manela, M. Segev, *Phys. Rev. Lett.* **2005**, *94*, 163902.

[57] O. Peleg, G. Bartal, B. Freedman, O. Manela, M. Segev, D. N. Christodoulides, *Phys. Rev. Lett.* **2007**, *98*, 103901.

[58] M. J. Ablowitz, S. D. Nixon, Y. Zhu, *Phys. Rev. A* **2009**, *79*, 053830.

[59] X. Wu, X. Li, R. Y. Zhang, X. Xiang, J. Tian, Y. Huang, S. Wang, B. Hou, C. T. Chan, W. Wen, *Phys. Rev. Lett.* **2020**, *124*, 075501.

[60] G. G. Pyrialakos, N. Schmitt, N. S. Nye, M. Heinrich, N. V. Kantartzis, A. Szameit, D. N. Christodoulides, *Nat. Commun.* **2020**, *11*, 2074.